

Redox-Improved Self-Assembled Monolayers for Inverted Perovskite Solar Cells

Received: 4 May 2025

Accepted: 7 November 2025

Published online: 12 December 2025



Meng Yuan^{1,2}, Yiyang Wang^{1,2}, Zhe Liu^{1,2}, Jinyuan Zhang¹,
Shucheng Qin¹, Minchao Liu^{1,2}, Zekun Chen^{1,2}, Yao Zhao^{2,3}, Jing Li⁴,
Xiaojun Li^{1,2}, Lei Meng^{1,2}✉ & Yongfang Li^{1,2,5}

Inverted perovskite solar cells (pero-SCs) utilizing nickel oxide (NiO_x)/self-assembled monolayer (SAM) as a hole transport layer (HTL) have demonstrated high power conversion efficiency (PCE). However, variations in the valence states of NiO_x on the surface create complexity in the growth of a high-quality SAM HTL. To address these challenges, a new SAM molecule MeOF-4SHCz is synthesized and utilized to target the Ni³⁺-rich regions on the NiO_x substrate. A redox reaction occurs at the interface and the oxidation product of MeOF-4SHCz forms a new S–O–Ni bonding at the Ni³⁺-rich regions. The application of the combined SAMs of MeOF-4SHCz and the regular SAM MeOF-4PACz can improve the overall coverage and uniformity of the SAM layer on NiO_x. As a result, the optimized inverted pero-SCs based on this redox-improved (ROI)-SAM HTL of MeOF-4SHCz/MeOF-4PACz = 4:1 (w/w) achieve a high PCE of 26.5% (certified as 26.28%) and improved stability with T₉₀ > 1000 hours.

Interface engineering is a crucial strategy in enhancing the overall performance of perovskite solar cells (pero-SCs), by improving the film morphology¹, charge carrier dynamics^{2,3}, and reducing interface charge recombination^{4,5}. Particularly, in inverted pero-SCs (or *p-i-n* pero-SCs), hole transport layer (HTL) at the bottom buried interface plays a critical role in the device performance. Among these HTLs, the self-assembled monolayer (SAM) has recently drawn great attention due to its simple structure, facile fabrication process and superior charge extraction efficiency^{6–9}. A typical SAM molecule consists of a *p*-type conjugated (such as a carbazole unit) terminal group, an alkyl spacer and an anchoring group¹⁰. The terminal group usually determines the energy level and surface wettability of the HTL, while the anchoring group shows significant influence on the resulting SAM coverage on substrate^{11–15}. Anchoring groups with –PO(OH)₂ exhibit higher substrate coverage compared to the alternatives like –COOH and –SO₃H, and are widely used in the molecular design of SAMs^{16–19}.

During the thermal annealing process, these SAM molecules bond to the metal oxide (MO) and form an organized monolayer. Among various metal oxides (MO), nickel oxide (NiO_x), a well-known *p*-type metal oxide, has been widely used as the substrate of the SAM HTL for its exceptional hole transport ability, chemical and thermal stability²⁰. With the application of the magnetron sputtering technology, the fabrication becomes suitable and widely utilized for large-scale production in industry²¹.

NiO_x exhibits strong chemical bonding with SAM²². Meanwhile, the deposition of SAM effectively passivates the defects on the NiO_x surface and optimizes the HTL/perovskite interface. Consequently, the combined HTL of NiO_x/SAM provides important opportunities for the improvement of the performance of *p-i-n* pero-SCs. You et al. modified NiO_x with hydrogen peroxide and created a more hydroxyl content surface, promoting the SAM anchoring on it²². Zhu et al. reported a SAM MeO-4PADBC in the NiO_x/SAM HTL with lowered voltage deficit

¹Beijing National Laboratory for Molecular Sciences, CAS Key Laboratory of Organic Solids, Institute of Chemistry, Chinese Academy of Sciences, Beijing 100190, China. ²School of Chemical Science, University of Chinese Academy of Sciences, Beijing 100049, China. ³Beijing National Laboratory for Molecular Science, Huairou Research Center, Institute of Chemistry, Chinese Academy of Sciences, Beijing 100190, China. ⁴Key Laboratory of Photochemical Conversion and Optoelectronic Materials, Technical Institute of Physics and Chemistry, Chinese Academy of Sciences, Beijing 100190, China. ⁵Laboratory of Advanced Optoelectronic Materials, Suzhou Key Laboratory of Novel Semiconductor Materials and Devices, College of Chemistry, Chemical Engineering and Materials Science, Soochow University, Suzhou, Jiangsu 215123, China. ✉e-mail: menglei@iccas.ac.cn

in the pero-SCs²³. Sargent et al. applied the NiO_x/SAM HTL into wide-bandgap pero-SCs in all perovskite tandem solar cell and achieved high performance²⁴. However, variations in the valence states of NiO_x on the surface create complexity in the growth of a high-quality SAM HTL. Meanwhile, the oxidation reaction caused by high-valent nickel species (Ni³⁺) in NiO_x can accelerate the decomposition of amine halides, detrimentally affecting both device performance and long-term stability^{25–27}.

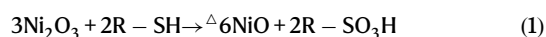
To simultaneously enhance the quality of the SAM and reduce the intrinsic reactivity of the NiO_x surface, comparing with the strategies mentioned above, we aimed to develop a dual-functional interfacial strategy. Given the strong oxidative nature of high-valence nickel species in NiO_x, we sought to exploit this property to promote the formation of a more homogeneous SAM layer. Specifically, we envisioned introducing a reducing agent that could react with NiO_x to passivate its surface while concurrently functioning as an HTL and facilitating the formation of a high-quality SAM layer.

Herein, we designed and synthesized a new SAM molecule 4-(3-fluoro-6-methoxy-9H-carbazol-9-yl)butane-1-thiol (MeOF-4SHCz), which is applied together with (4-(3-fluoro-6-methoxy-9H-carbazol-9-yl)butyl)phosphonic acid (MeOF-4PACz) as a combined HTL²⁸. Due to the reducibility of thiol groups, MeOF-4SHCz can serve as an effective reducing agent to reduce the Ni³⁺-rich regions on the surface of the NiO_x substrate. The oxidation product of 4-(3-fluoro-6-methoxy-9H-carbazol-9-yl)butane-1-sulfonic acid (MeOF-4SACz) could form a new S-O-Ni bond at the Ni³⁺ region, together with the P-O-Ni bond at the Ni²⁺ region, improving the overall quality and coverage of SAM on the NiO_x substrate. Moreover, the redox reaction causes the reduction of Ni³⁺ on the NiO_x surface and hence lowers the reactivity between the NiO_x and perovskite interface, which is beneficial to improving the photovoltaic performance of pero-SCs. As a result, the device based on the redox-improved (ROI)-SAM reaches a higher PCE of 26.5% (certified as 26.28%), and a better stability of T₉₀ > 1000 h at the maximum power point (MPP) under continuous 1 sun illumination.

Results

Mechanisms for ROI-SAM

The molecular structure of MeOF-4SHCz is presented in Fig. 1a, and the synthesis procedures of MeOF-4SHCz are described in the Methods section. The molecular structures were further confirmed by nuclear magnetic resonance (NMR) spectroscopy as shown in Supplementary Figs. 1–7. To investigate the interaction between the MeOF-4SHCz and the NiO_x substrate, X-ray photoelectron spectroscopy (XPS) measurements were performed. We analyzed the XPS spectra to examine the valence states of the elements, and the detailed XPS peak fitting data are listed in Supplementary Tables 1–7. The MeOF-4SHCz SAM was deposited onto the NiO_x substrate, before annealing, two distinct peaks were observed in S 2*p* spectrum at binding energies of 163.2 eV and 164.3 eV, corresponding to the S²⁻ species from thiol groups²⁹. Notably, after annealing at 100 °C for 10 minutes, a new peak appeared in S 2*p* spectrum at binding energy of 167.5 eV (see Fig. 1b, Supplementary Tables 1 and 2), which is also reported in the previous study on the adsorption of alkyl mercaptan on the NiO_x surface³⁰. To determine the oxidation product, we conducted electrospray ionization Fourier-transform ion cyclotron resonance mass spectrometry (ESI-FTICR-MS) based on the mixture of NiO_x nanoparticles and MeOF-4SHCz. The substance with mass-to-charge (*m/z*) of 350.1 was detected, suggesting the formation of MeOF-4SACz molecules with –SO₃H groups (Supplementary Fig. 8). Therefore, we deduce that the –SH group in MeOF-4SHCz is oxidized by Ni³⁺ into –SO₃H group, as illustrated by the following chemical equation:



where R represents the 3-fluoro-6-methoxy-9H-carbazol (MeOF-Cz). Based on the above redox reaction, we further synthesized the MeOF-4SACz and measured its XPS spectrum. It exhibits a binding energy of 167.7 eV (Fig. 1c), closely matching the new peak appeared in S 2*p* spectrum mentioned above. Moreover, for the MeOF-4SHCz treated NiO_x film, the existence of –SO₃H groups can also be observed by photo-induced force microscopy (PiFM) (Supplementary Fig. 9). This oxidation process is shown in Fig. 1d. The –SO₃H group generated from oxidation can serve as an additional anchoring group on the NiO_x surface.

As MeOF-4SHCz is co-applied with MeOF-4PACz on the NiO_x substrate, it is important to investigate the binding preference of each SAM on different Ni species (Ni²⁺, Ni³⁺). Therefore, we calculated the reaction energy between SAM and NiO_x surface (Fig. 1d, e)^{31–34}. The results show that there is a tridentate bind mode at NiO surface because of the thermodynamically favorable configuration with the lowest total energy, while a bidentate mode at Ni₂O₃ surface due to the larger lattice spacing, and this larger lattice spacing limits the interaction between the anchor group and the substrate (Supplementary Fig. 10, Supplementary Tables 3–4). For the MeOF-4PACz, the reaction energy with NiO is –0.80 eV, and that with Ni₂O₃ is –1.00 eV, indicating no significant preference between the two Ni species. For the MeOF-4SHCz, the reaction energy with NiO is –0.09 eV, which suggests it hardly interacts with Ni²⁺. However, on Ni₂O₃, MeOF-4SHCz preferentially undergoes oxidation with a reaction energy of –5.25 eV, which is significantly lower than that of MeOF-4PACz with Ni₂O₃, indicating a much stronger driving force for the reaction of MeOF-4SHCz with Ni₂O₃ during the self-assembly process. As a result, the MeOF-4SHCz strengthens the binding of the SAM to the Ni³⁺-rich regions, and improves the quality of the SAM layer on NiO_x substrate.

As the thiol group in MeOF-4SHCz is oxidized to higher valence states, the valence state of the oxidant NiO_x also changes. The peak fitting and analysis of Ni in the XPS spectra were performed^{25,27,35,36}. The content of NiO species was calculated to evaluate the Ni²⁺ content, and the total content of higher valence species was considered as Ni³⁺ content. The binding energy of different Ni species is listed in Supplementary Table 5. For bare NiO_x, as shown in Supplementary Fig. 11 and Supplementary Table 6, the integration results of the peak fitting show that the content of Ni³⁺ is 78.2%. When MeOF-4SHCz is deposited on NiO_x, as shown in Fig. 1f and Supplementary Table 6, the Ni³⁺ content decreases to 75.3%. This change suggests that the Ni³⁺ species on the surface is reduced to a lower oxidation state. However, when the regular MeOF-4PACz is deposited on NiO_x, the content of Ni³⁺ remained 78.1% and shows almost no change, which means the –PO(OH)₂ group barely influences the valence state of the NiO_x surface. The results also indicate that the –SH groups are more inclined to react with Ni³⁺ than –PO(OH)₂ groups, which makes MeOF-4SHCz an effective SAM to target the Ni³⁺-rich region on the NiO_x substrate, potentially contributing to a more homogeneous SAM layer. Considering that the reaction mainly occurs at the surface, to further investigate the oxidation of Ni³⁺ species, Ni₂O₃ powder was mixed with the MeOF-4SHCz powder and XPS measurements were performed. The results show about 47% of MeOF-4SHCz oxidized to MeOF-4SACz, which confirms the surface oxidative role of the Ni³⁺ (Supplementary Fig. 12). And this process can be illustrated as Fig. 1g.

Measurements of kinetic process of the SAMs were conducted to characterize the oxidation influence of HTL on the perovskite layer. For simplicity, the MeOF-4PACz SAM is named as “Pristine-SAM”. The X-ray diffraction (XRD) analysis reveals that the perovskite layers coated on the ROI-SAM substrates exhibit a slight decrease in the intensity ratio of the PbI₂ peak to the FAPbI₃ (100) (Fig. 1h). And the tendency is shown in the inset, with the ratio of 0.128 for bare NiO_x, 0.103 for the Pristine-SAM, and 0.091 for the ROI-SAM, respectively (Supplementary Table 7). As the three samples have the same perovskite composition, the reduced PbI₂ formation corresponds to a

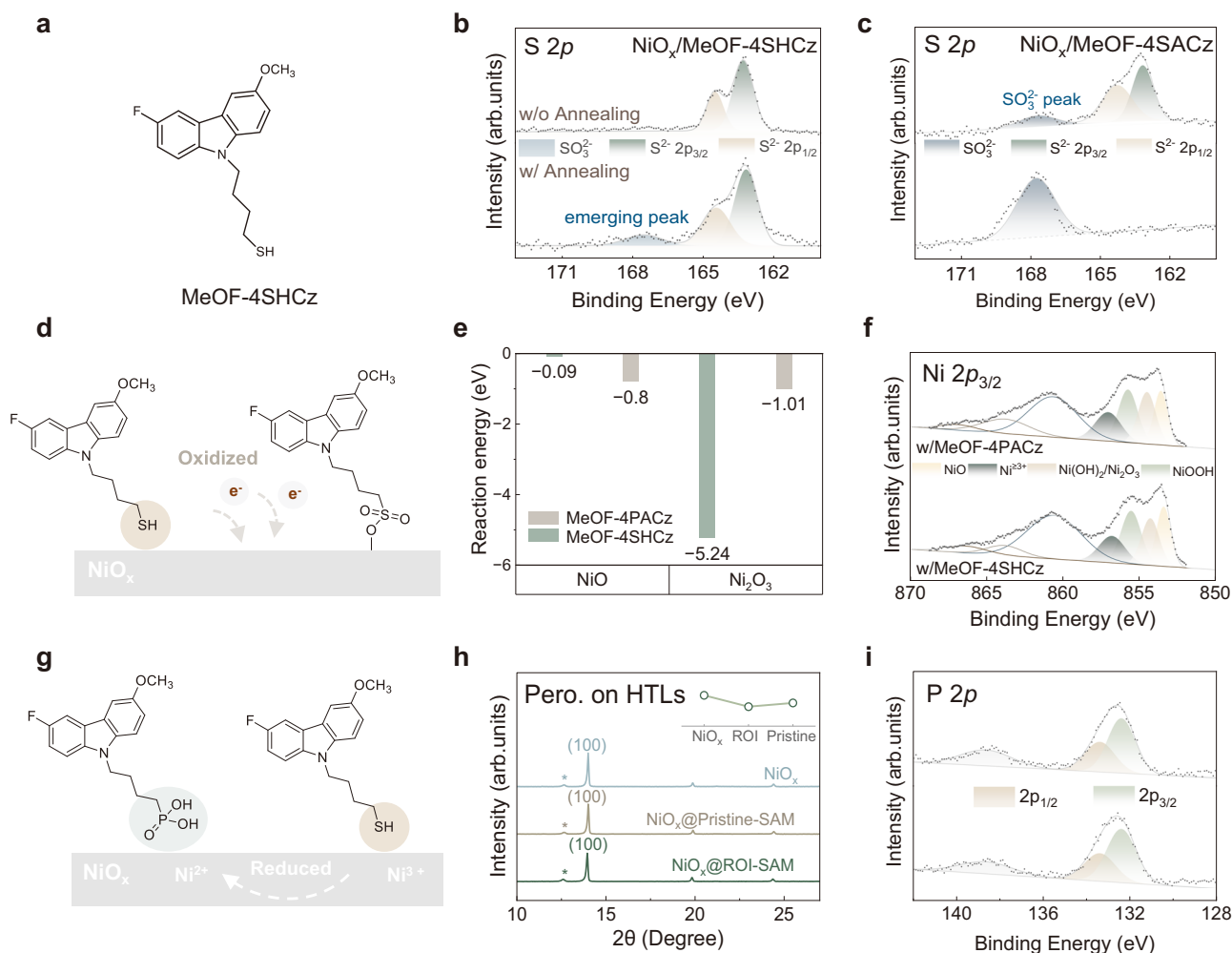
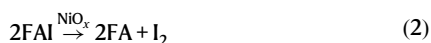


Fig. 1 | Redox reaction at the NiO_x-perovskite interface. **a** Chemical structure of MeOF-4SHCz. **b** S 2p XPS spectra and fitted peaks of the NiO_x/MeOF-4SHCz samples before and after thermal annealing. The fitted components include S²⁻ 2p_{3/2} (green), S²⁻ 2p_{1/2} (brown), and SO₃²⁻ (blue). **c** S 2p XPS spectra and fitted peaks of NiO_x/MeOF-4SHCz (thermal annealed) and MeOF-4SACz. The fitted components include S²⁻ 2p_{3/2} (green), S²⁻ 2p_{1/2} (brown), and SO₃²⁻ (blue). **d** Schematic illustration of the oxidation process. **e** Reaction energy of MeOF-4PACz and MeOF-4SHCz with NiO and Ni₂O₃, respectively. **f** Ni 2p XPS spectra and fitted peaks of NiO_x after

treatment with MeOF-4PACz and MeOF-4SHCz. The fitted components include NiO (yellow), Ni(OH)₂/Ni₂O₃ (brown), NiOOH (green) and Ni³⁺ species (dark green). **g** Schematic illustration of the reduction process. **h** XRD spectra of perovskite coated on NiO_x, NiO_x/Pristine-SAM and NiO_x/ROI-SAM. The inset presents the ratio of the intensity of the PbI₂ peak and the FAPbI₃ (100) peak. **i** P 2p XPS spectra and fitted peaks of the NiO_x/MeOF-4PACz (top) and NiO_x/MeOF-4SHCz samples, respectively. The fitted components include P 2p_{3/2} (green) and P 2p_{1/2} (brown). Source data are provided as a Source Data file.

lower loss of ammonium salts, which indicates the less oxidation of I⁻. We performed additional analyses to directly investigate the interfacial degradation (Supplementary Fig. 13). Specifically, we deposited FAI onto the NiO_x layer and the NiO_x/MeOF-4SHCz layer, and found the formation of the neutral FA molecule in NiO_x/FAI sample. To figure out the chemical transformation, we immersed the sample into anhydrous toluene and performed UV measurement. The UV-vis absorption spectrum shows a peak at -500 nm, characteristic of molecular iodine, confirming the oxidation of I⁻ during the process. The reaction can be summarized as



However, the NiO_x/MeOF-4SHCz sample shows no FA molecule generated. As a result, the deposition of MeOF-4SHCz on NiO_x could reduce the reactivity between NiO_x and perovskite active layer, thereby suppressing the oxidation of perovskite components and potentially enhancing the long-term stability of the corresponding pero-SCs.

As shown in Fig. 1i and Supplementary Table 8, the addition of MeOF-4SHCz did not affect the binding energy of phosphorus, indicating the -SH group did not cause obvious change to the bonding between -PO(OH)₂ and NiO_x layer in the rest Ni²⁺-rich regions. Eventually, MeOF-4SHCz can serve as an effective reducing agent and effectively reduce the Ni³⁺-rich regions on the NiO_x substrate, which may contribute to a more uniform SAM layer.

Distribution of SAM in devices

Kelvin probe force microscopy (KPFM) was employed to examine the potential distribution of SAM on the NiO_x layer. As illustrated in Fig. 2a and b, the sample with ROI-SAM displays a more uniform potential distribution with a smaller standard deviation than that of the sample with the Pristine-SAM, with 22.6 mV for Pristine-SAM and 14.5 mV for ROI-SAM, which suggests that the ROI-SAM exhibits a more uniform SAM layer³⁷. Additionally, the conductive atomic force microscopy (c-AFM) demonstrates that the ROI-SAM sample (root mean square roughness (RMS) equals 0.134 nA) has a more uniform distribution than the Pristine-SAM sample (RMS = 0.197 nA) as shown in Fig. 2c, d.

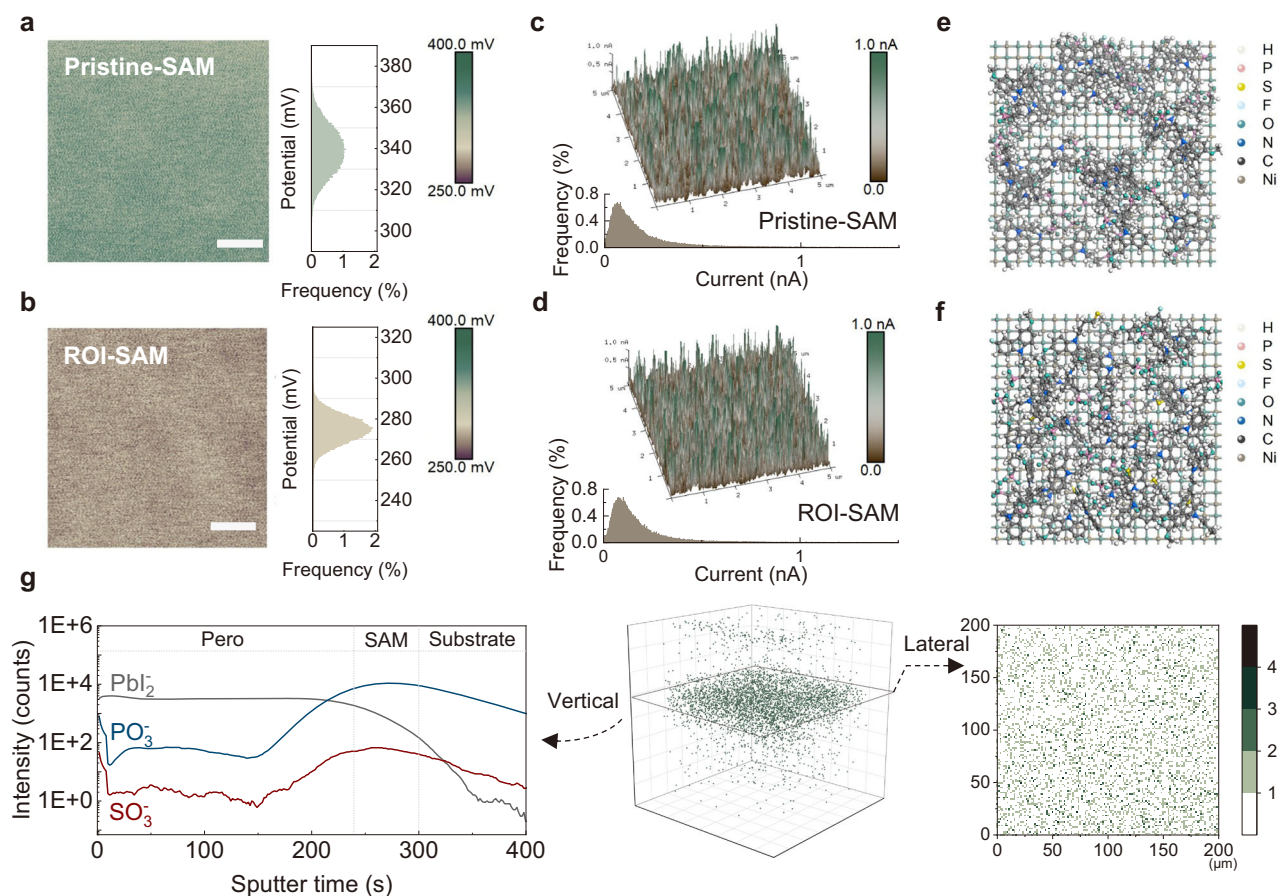


Fig. 2 | Distribution of SAM on NiO_x . KPFM surface potential maps and corresponding potential histograms of the Pristine-SAM (a) and ROI-SAM (b) on NiO_x substrates. Scale bar: 1 μm . The mean surface potential is 339.2 mV for Pristine-SAM and 274.2 mV for ROI-SAM. The corresponding standard deviations are 22.6 mV and 14.5 mV, respectively. c-AFM current maps and corresponding current histograms of Pristine-SAM (c) and ROI-SAM (d) on NiO_x substrates. The average current is 0.181 nA for Pristine-SAM and 0.177 nA for ROI-SAM. The RMS values of two

samples are 0.197 and 0.134, respectively. Top views of equilibrated molecular representation of Pristine-SAM (e) and ROI-SAM (f). g TOF-SIMS depth profiles of selected ions and 3D imaging of SO_3^- (green dot) of the perovskite deposited on the NiO_x /ROI-SAM substrate. The sputter time and the true vertical depth of the perovskite layer are not scaled. The film was fabricated based on an ITO substrate. Source data are provided as a Source Data file.

The results indicate that MeOF-4SHCz additive effectively improves the SAM uniformity on the NiO_x substrate, which is favorable for the charge transfer in the corresponding pero-SCs. Meanwhile, the contact potential difference (CPD) of the ROI-SAM HTL is 274.2 mV, slightly lower than that (339.2 mV) of the Pristine-SAM sample (Fig. 2a, b), indicating that the ROI-SAM HTL has a deeper Fermi level with improved electron-blocking capability. Additionally, we performed conductivity measurements on both ROI-SAM and Pristine-SAM samples (Supplementary Fig. 14). The conductance showed a negligible change from 0.451 S to 0.439 S, indicating that the surface reaction had little impact on the bulk conductivity. Ultraviolet photoelectron spectroscopy (UPS) measurements were conducted to further confirm the energy level of the HTLs (Supplementary Fig. 15), with the data shown in Supplementary Table 9. The work function calculated from UPS curves of ROI-SAM sample is 5.38 eV, slightly higher than the Pristine-SAM sample of 5.31 eV, which is consistent with the CPD data.

To understand the self-assembly process of the Pristine-SAM and ROI-SAM systems, we performed molecular dynamics simulations to reveal the interaction between MeOF-4PACz and MeOF-4SHCz on the NiO_x substrate during self-assembly³⁸. The detailed kinetic processes are presented in Supplementary Figs. 16 and 17. From 20 ps to 100 ps, phosphate groups tend to form clusters due

to hydrogen-bond interactions, leading to aggregation in the solution. After introducing MeOF-4SHCz with thiol groups, the dispersion of phosphate groups improves, and the number of clusters decreases at equilibrium, this improvement in solution dispersion facilitates uniform adsorption on the substrate. With the incorporation of MeOF-4SHCz, the SAM precursor solution also exhibits improved homogeneity, as shown in Fig. 2e and f, which is beneficial to the homogeneity of the formation of the SAM. When annealing, MeOF-4SHCz undergoes oxidation to form $-\text{SO}_3\text{H}$ groups, which anchor onto the NiO_x substrate and function as part of the HTL, improving the overall quality of the SAM layer.

Time-of-flight secondary ion mass spectrometry (TOF-SIMS) was performed to study the spatial distribution of the SAM in the device (Fig. 2g). The perovskite precursor was dissolved in DMF/NMP = 6:4 (v/v) to diminish trace DMSO in perovskite film, and the sulfur content is entirely attributed to the $-\text{SO}_3\text{H}$ group in the SAM. When conducting the TOF-SIMS measurement, the $-\text{SO}_3\text{H}$ group is detected as SO_3^- . It was concentrated at the same depth as PO_3^- (see Supplementary Fig. 18) and remains resistant to washing and the annealing of the perovskite precursor solution, which suggests the bonding of the $-\text{SO}_3\text{H}$ on the NiO_x substrate. Moreover, the SO_3^- lateral distribution driven by the redox reaction is found to be uniform, which also confirms the overall coverage of the SAM on the NiO_x .

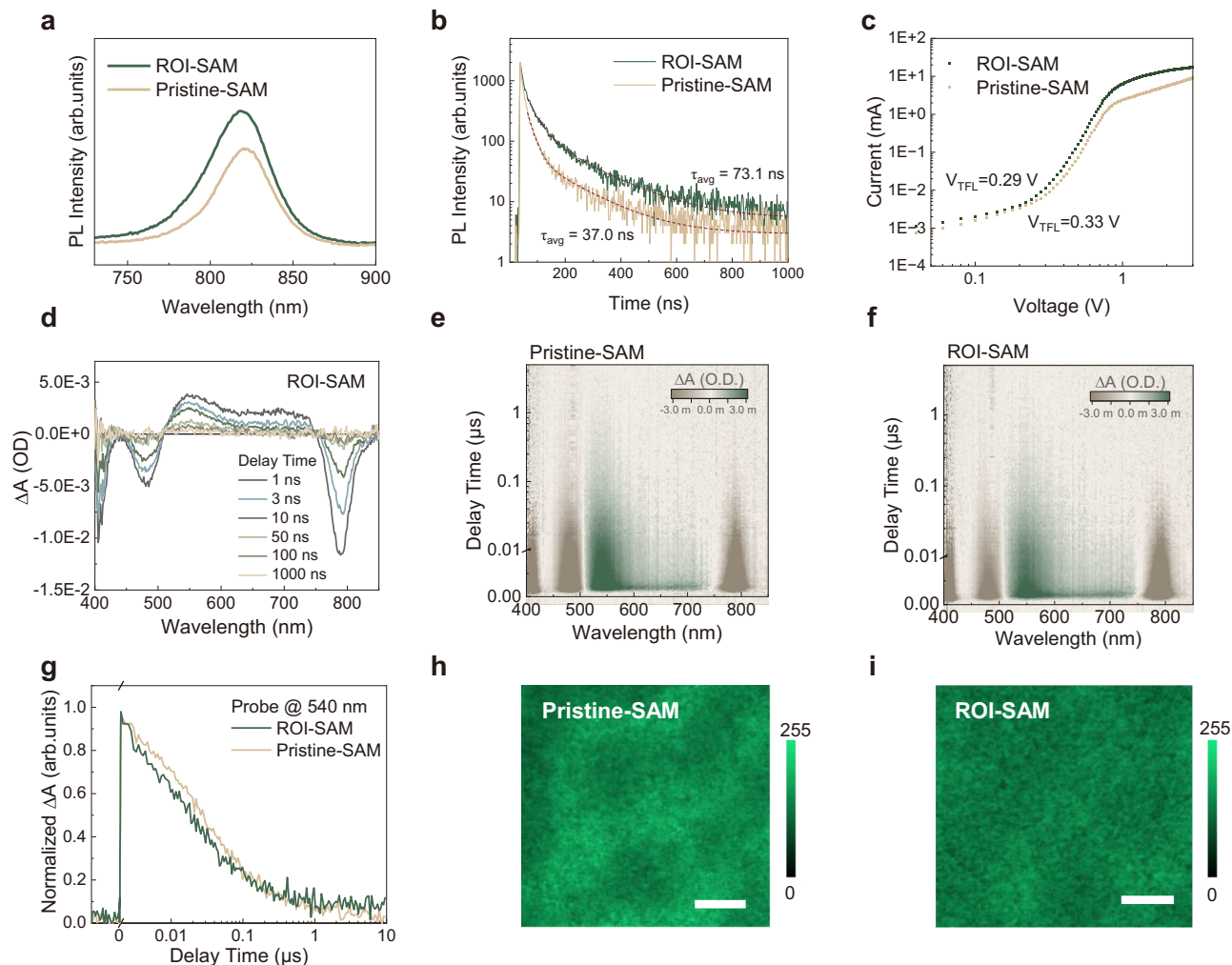


Fig. 3 | Characteristics of SAM layers and the corresponding perovskite films.

PL and TRPL spectra of perovskite films deposited on NiO_x/Pristine-SAM (a) and NiO_x/ROI-SAM (b) substrates, respectively. The excitation light was incident from the ITO side. c Dark Current density-voltage curves using the SCLC model for hole-only devices: ITO/NiO_x/SAM/Perovskite/Spiro-OMeTAD/Ag, with Pristine-SAM or ROI-SAM. The hole mobility in the ROI-SAM based device is $2.95 \times 10^{-3} \text{ cm}^2 \cdot \text{V}^{-1} \cdot \text{s}^{-1}$ while the Pristine-SAM device is $1.17 \times 10^{-3} \text{ cm}^2 \cdot \text{V}^{-1} \cdot \text{s}^{-1}$. d Nanosecond transient

absorption spectra of Pristine-SAM. 2D Nanosecond transient absorption spectra of Pristine-SAM (e) and ROI-SAM (f), respectively. g Kinetic traces probing at 540 nm for the ESA of carriers in Pristine-SAM and ROI-SAM based perovskite films. The pump light was incident from the ITO side. PL mapping of perovskite film coated on Pristine-SAM (h) and ROI-SAM (i) HTL, respectively. scale bar, 10 μm . Source data are provided as a Source Data file.

Optoelectronic properties of the SAM layer and Perovskite films

To investigate the charge recombination properties and charge-carrier dynamics at the buried perovskite interface, we measured steady-state photoluminescence (PL) spectra (Fig. 3a) and time-resolved photoluminescence (TRPL) (Fig. 3b, Supplementary Fig. 19 and Supplementary Table 10). The perovskite film coated on the ROI-SAM (ROI-SAM sample) exhibits higher PL intensity compared to that on the Pristine-SAM HTL (Pristine-SAM sample), indicating the reduced non-radiative charge recombination. The TRPL spectrum of NiO_x/ROI-SAM displays a longer decay time (73.1 ns) compared to that (37.0 ns) of the Pristine-SAM sample, which suggests reduced non-radiative charge recombination loss at the interface^{39,40}. Space charge limited current (SCLC) technique was employed to characterize the defect density⁴¹ (Fig. 3c). The trap-filled-limit voltage (V_{TFL}) extracted from the ROI-SAM sample is 0.29 V and smaller than that (0.33 V) of the Pristine-SAM sample, which means a lower trap density. This reduction is likely due to the higher quality of the buried SAM layer, which facilitates better crystallization and growth of the perovskite film, thereby reducing interfacial defects, consistent with the observations from the decay time of TRPL spectrum.

The nanosecond transient absorption (TA) spectra measurements were also conducted to investigate the exciton dissociation and recombination dynamics of different HTLs (Fig. 3d, Supplementary Fig. 20). A pump wavelength of 488 nm was used to selectively excite the film. As shown in the 2D spectra in Fig. 3e, f, both samples exhibit similar transient absorption features. Between 520 nm and 720 nm, a broad excited state absorption (ESA) peak centered at 540 nm was observed. We then compared the transient kinetics at the wavelength of 540 nm^{42,43}, as shown in Fig. 3g. The ROI-SAM-based film exhibited a rapid decay before 0.1 μs , likely due to the more effective charge extraction, which decreases the number of charge carriers in the perovskite film. After 1 μs , this curve decays more slowly than that of the Pristine-SAM sample.

Moreover, PL mapping of the ROI-SAM HTL exhibits a more uniform PL emission (Fig. 3h, i), which is likely contributing to the improved buried interface. We further investigated the morphology of the perovskite layer using scanning electron microscopy (SEM) and atomic force microscopy (AFM). Compared to the film coated on Pristine-SAM, the ROI-SAM-based film exhibits larger grains (Supplementary Fig. 21), and reduced RMS (Supplementary Fig. 22). These

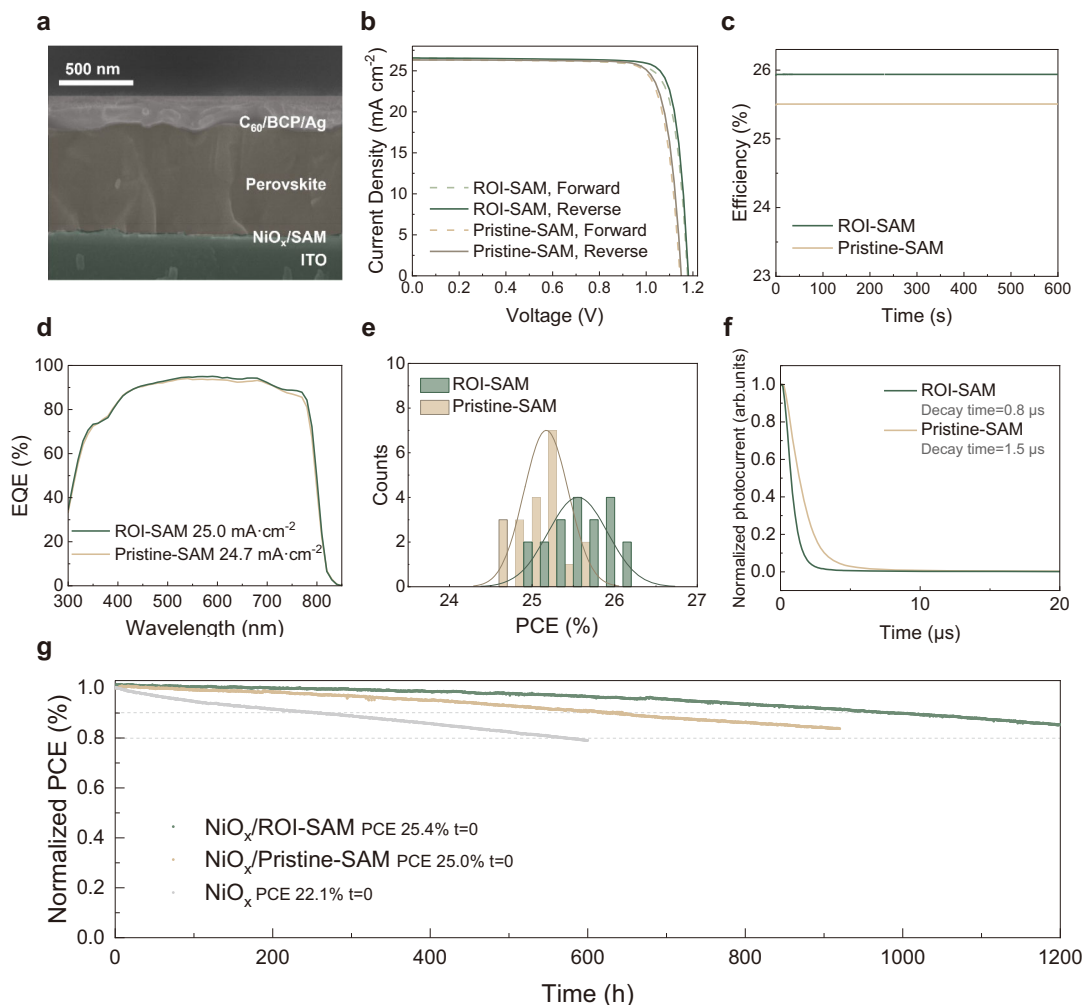


Fig. 4 | Photovoltaic performance of perovskite solar cells. **a** Cross-sectional SEM image of the ROI-SAM based pero-SC. **b** J - V characteristics curves of the pero-SCs using Pristine-SAM or ROI-SAM as HTLs under forward and reverse scans (device area: 0.09 cm^2), under the illumination of AM1.5 G, 100 mW cm^{-2} . **c** Steady-state PCEs of the pero-SCs using Pristine-SAM or ROI-SAM as HTLs. **d** EQE curves of

the pero-SCs using Pristine-SAM or ROI-SAM as HTLs. **e** Distribution of the PCEs of the pero-SCs using Pristine-SAM or ROI-SAM as HTLs. **f** Transient photocurrent plots of the devices with $\text{NiO}_x/\text{Pristine-SAM}$ or $\text{NiO}_x/\text{ROI-SAM}$ HTL. **g** MPP tracking of the encapsulated pero-SCs using Pristine-SAM or ROI-SAM as HTLs (LED lamp, 100 mW cm^{-2} , 25°C , 30% RH). Source data are provided as a Source Data file.

results also confirm that, after using ROI-SAM as HTL, the perovskite layer exhibits a more uniform morphology, which is beneficial to the interfacial contact and improves the device performance.

Photovoltaic performance of the *p-i-n* pero-SCs

We fabricated devices and studied the photovoltaic performance of pero-SCs utilizing the Pristine-SAM or ROI-SAM as HTLs. The device structure of the pero-SCs studied in this work is shown in the cross-sectional SEM image in Fig. 4a, with the architecture of ITO/ $\text{NiO}_x/\text{SAM}/\text{perovskite}/\text{C}_{60}/\text{BCP}/\text{Ag}$ [ITO, indium tin oxide; BCP, 2,9-Dimethyl-4,7-diphenyl-1,10-phenanthroline]. The concentration of MeOF-4SHCz in the ROI-SAM solution was optimized to be $0.25 \text{ mg}\cdot\text{mL}^{-1}$, and the concentration of MeOF-4PACz is $1 \text{ mg}\cdot\text{mL}^{-1}$ (weight ratio of MeOF-4SHCz/MeOF-4PACz is 1:4). The effect of the MeOF-4SHCz concentration on photovoltaic performance parameters of the pero-SCs is presented and compared in Supplementary Fig. 23. It is shown that the PCE of the pero-SCs based on the ROI-SAM increases with the MeOF-4SHCz concentration rising from 0 to $0.25 \text{ mg}\cdot\text{mL}^{-1}$. However, as the MeOF-4SHCz concentration is further increased to $0.5 \text{ mg}\cdot\text{mL}^{-1}$, the device performance declines, which is likely due to the hindered bonding between MeOF-4PACz and NiO_x by excessive MeOF-4SHCz.

The current density (J)-voltage (V) characteristic curves of pero-SCs under forward and reverse scans are illustrated in Fig. 4b. The

optimized ROI-SAM based devices show an improved J_{sc} of $26.6 \text{ mA}\cdot\text{cm}^{-2}$, V_{oc} of 1.18 V and FF of 84.5% in comparison with the Pristine-SAM based devices showing the slightly lower J_{sc} of $26.4 \text{ mA}\cdot\text{cm}^{-2}$, V_{oc} of 1.15 V and FF of 83.2%, leading to an enhanced PCE from 25.3% for the Pristine-SAM based devices to 26.5% for the ROI-SAM based devices (Supplementary Table 11, certified PCE of 26.28%, Supplementary Fig. 24). The steady-state PCEs of the pero-SCs using Pristine-SAM or ROI-SAM as HTLs were 25.5% and 25.9%, respectively, as shown in Fig. 4c. In addition, the J_{sc} value from the external quantum efficiency (EQE) measurements was integrated to be $24.7 \text{ mA}\cdot\text{cm}^{-2}$ for the Pristine-SAM based devices and $25.0 \text{ mA}\cdot\text{cm}^{-2}$ for the ROI-SAM based devices, as shown in Fig. 4d. The statistical device parameters are illustrated in Fig. 4e, which indicates that the ROI-SAM based devices show good reproducibility, likely due to the improved uniformity of the buried SAM layer.

The charge transfer dynamics in the pero-SCs were investigated by transient photocurrent (TPC) measurement⁴⁴ (Fig. 4f). The photocurrent delay time of the device based on ROI-SAM is $0.8 \mu\text{s}$ and smaller than that ($1.5 \mu\text{s}$) of the Pristine-SAM, suggesting more effective charge carrier extraction. In Supplementary Fig. 25, the exponential factor (α) of ROI-SAM device obtained from the slope of the logarithmic J_{sc} and logarithmic light intensity is closer to 1, suggesting better charge transport and reduced recombination of ROI-SAM HTL.

Besides the increased efficiency, we evaluated the long-term operational stability of the encapsulated device by tracking the maximum power point (MPP) under 1 sun illumination at 25 °C and 30% relative humidity (Fig. 4g). The ROI-SAM based devices retained 90% of their initial efficiency (T_{90}) after about 1000 hours. In contrast, the Pristine-SAM based control devices maintained 81% of their initial PCE under the same conditions, while the unmodified NiO_x -based devices exhibited the T_{80} around 600 hours, which shows the enhanced stability of the ROI-SAM-based devices. We then conducted thermal tests at 85 °C under N_2 atmosphere. The ROI-SAM devices showed improved thermal tolerance ($T_{90} > 576$ h) compared to the control ($T_{90} = 72$ h) and Pristine-SAM ($T_{90} = 312$ h) devices (Supplementary Fig. 26). The improved long-term efficiency is attributed to the improved SAM layer and better interfacial contact with the perovskite active layer, and the decomposition of perovskite caused by the oxidation of Ni^{3+} can be mitigated. These results indicate that the ROI-SAM HTL with weight ratio of MeOF-4SHCz/MeOF-4PACz = 1:4 is an effective strategy for enhancing the operational stability of *p-i-n* pero-SCs.

Discussion

In conclusion, we present a ROI-SAM strategy utilizing the difference in the reaction driving forces between -SH group and -PO(OH)₂ group to target the Ni^{3+} -rich and Ni^{2+} -rich regions on the NiO_x substrate, respectively. The -SH-functionalized SAM molecule MeOF-4SHCz can be oxidized and effectively form bonds with the high-valence region of NiO_x during annealing, and the valence states of NiO_x becomes more homogeneous due to the redox reaction. This strategy provides a facile approach to enhance the overall quality and uniformity of SAM/ NiO_x HTL in the inverted pero-SCs.

Methods

Materials

Cesium iodide (CsI, 99.9%), dimethyl formamide (DMF, anhydrous) and dimethyl sulfoxide (DMSO, anhydrous) were purchased from Sigma-Aldrich. Formamidinium iodide (FAI, 99.5%), methylammonium iodide (MAI, 99.5%), lead iodide (PbI_2 , 99.9%), lead chloride (PbCl_2 , 99.9%), 1,3-Propyldiammonium diiodide (PDADI) and C_{60} were purchased from Xi'an Yuri Solar Co. All materials were used as received without further purification. ITO substrates were purchased from Suzhou Shangyang Solar Technology Co.

Synthesis of MeOF-4PACz

MeOF-4PACz was obtained in our laboratory as published previously.

Synthesis of MeOF-4SHCz

Supplementary Fig. 1 shows the synthetic route of MeOF-4SHCz, and it was synthesized by the following steps. MeOF-4C-Br (500 mg, 1.432 mmol) and thiourea (163.6 mg, 2.149 mmol) were dissolved in EtOH (20 mL) in a two-neck round-bottom flask. The mixture was refluxed at 80 °C for 20 h under argon protection. Subsequently, an aqueous solution of KOH (4.9 g in 7 mL H_2O) was added into the flask and the resulting mixture was refluxed for another 9 h. After cooling to room temperature, HCl was added to adjust the pH of the solution to 4. The mixture was then extracted with dichloromethane (50 mL×3) and the organic phase was purified by column chromatography on silica gel using dichloromethane/petroleum ether (1/3, v/v) as the eluent. As a result, a white powder of MeOF-4SHCz (212 mg, 49% yield) was obtained. ¹H NMR (400 MHz, DMSO-*d*₆) δ 7.98 (dd, *J* = 9.4, 2.6 Hz, 1H), 7.75 (d, *J* = 2.5 Hz, 1H), 7.60 – 7.48 (m, 2H), 7.27 (td, *J* = 9.1, 2.6 Hz, 1H), 7.12 (dd, *J* = 9.0, 2.6 Hz, 1H), 4.36 (t, *J* = 7.0 Hz, 2H), 3.85 (s, 3H), 2.52–2.42 (m, 2H), 2.21 (t, *J* = 7.8 Hz, 1H), 1.82 (p, *J* = 7.1 Hz, 2H), 1.53 (p, *J* = 7.3 Hz, 2H). ¹³C NMR (101 MHz, DMSO-*d*₆) δ 157.77, 155.47, 153.51, 137.44, 136.32, 122.78, 122.68, 122.48, 122.44, 116.08, 113.74, 113.49, 110.81, 110.73, 110.64, 106.52, 106.28, 103.99, 56.17, 56.10, 42.46,

40.63, 40.42, 40.21, 40.00, 39.79, 39.58, 39.37, 31.28, 27.85, 27.76, 26.57, 23.95. ESI-FTICR-MS, Calcd for $\text{C}_{17}\text{H}_{18}\text{FNOS}$ (M-H): 302.10149 Found: 302.10237.

Synthesis of MeOF-4SACz

Supplementary Fig. 2 shows the synthetic route of MeOF-4SACz, and it was synthesized by the following steps. Sodium hydride (71 mg, 3.04 mmol) was carefully added to a solution of MeOF core (500 mg, 2.33 mmol) in 30 mL of anhydrous THF at 0 °C. After stirring for 1 h, 1,4-butanediol (414 mg, 3.04 mmol) was added and the reaction mixture was refluxed for 24 h. The resulting solid was recovered by filtration and washed with acetone repeatedly to afford product as a slightly yellow powder (0.66 g, 81% yield). ¹H NMR (400 MHz, DMSO-*d*₆) δ 7.96 (dd, *J* = 9.4, 2.6 Hz, 1H), 7.74 (d, *J* = 2.5 Hz, 1H), 7.62–7.50 (m, 2H), 7.25 (td, *J* = 9.2, 2.6 Hz, 1H), 7.11 (dd, *J* = 8.9, 2.6 Hz, 1H), 4.34 (t, *J* = 7.1 Hz, 2H), 3.85 (s, 3H), 2.48 – 2.40 (m, 2H), 1.80 (p, *J* = 7.3 Hz, 2H), 1.65–1.53 (m, 2H). ¹³C NMR (101 MHz, DMSO-*d*₆) δ 157.73, 155.42, 153.46, 137.46, 136.36, 122.71, 122.62, 122.42, 122.38, 116.06, 113.70, 113.46, 110.88, 110.80, 110.71, 106.44, 106.20, 103.98, 56.19, 56.11, 51.55, 42.90, 40.61, 40.41, 40.29, 40.20, 39.99, 39.78, 39.57, 39.36, 28.43, 23.19. ESI-FTICR-MS, Calcd for $\text{C}_{17}\text{H}_{17}\text{FNO}_4\text{S}$ (M-H): 351.09406 Found: 350.08696.

Device fabrication

The patterned ITO glass substrates were sonicated with detergent, deionized water, acetone and isopropanol for 30 min sequentially. After the ultraviolet ozone treatment for 30 min, NiO_x (15 mg·mL⁻¹) were spin-coated on the substrate at 3,000 rpm for 30 s and annealed at 150 °C for 15 minutes in the ambient air. Then the controlled condition (1 mg·mL⁻¹ MeOF-4PACz) and target condition (1 mg·mL⁻¹ MeOF-4PACz and 0.25 mg·mL⁻¹ MeOF-4SHCz) solutions were spin-coated on NiO_x at 3,000 rpm for 30 s and then annealed in inert gas at 100 °C for 10 min respectively. $\text{Cs}_{0.05}\text{FA}_{0.9}\text{MA}_{0.05}\text{PbI}_3$ was prepared according to the stoichiometric ratio with solvent of DMSO: DMF (v/v = 1/5) as the perovskite precursor, with excessive 5% PbCl_2 and MAI addition. The 1.8 M perovskite precursor solution was spin-coated at 5,000 rpm for 30 s with an acceleration of 5,000 rpm s⁻¹ and at the 15 s, 800 μL diethyl ether poured onto the substrate. The perovskite films were annealed at 100 °C for 30 min in the N_2 atmosphere. 0.5 mg mL⁻¹ PDADI was spin-coated at 5,000 rpm for 30 s and then annealed at 100 °C for 10 min. Finally, C_{60} (30 nm)/BCP (8 nm)/Ag (100 nm) were deposited by thermal evaporation under a pressure of 2×10^{-6} torr. The devices were controlled by a mask with an area of 0.09 cm² during the *J-V* measurement.

Characterization of SAM and perovskite films

The ¹H and ¹³C nuclear magnetic resonance spectroscopy was recorded on Bruker AVANCE 400 MHz spectrometer at 300 K. Chemical shifts (δ) are reported relative to tetramethylsilane (TMS) as an internal standard. High-resolution mass spectra were recorded on a Bruker solarix Fourier-transform ion cyclotron resonance mass spectrometer (FTICR-MS) equipped with an electrospray ionization (ESI) source operating in negative-ion mode. Fourier-transform Infrared (FTIR) Spectroscopy was recorded on Bruker VERTEX 70 v, and UV-Vis absorption spectra were obtained on PerkinElmer Lambda 1050 +.

X-ray Photoelectron spectroscopy (XPS) data and Ultraviolet photoelectron spectroscopy (UPS) were measured by Kratos AXIS ULTRA DLD spectrometer. Non monochromatic He I (21.22 eV) source was used as an excitation source. Gold was used as reference. The bias voltage applied during the test is -9 V. X-ray diffraction (XRD) was measured with PANalytical Empyrean X-ray diffractometer with Cu Kα radiation at the scan rate of 2° min⁻¹.

Photo-induced force microscopy (PiFM) results were acquired using a Vista Scope microscope from Molecular Vista, inc., from Songshan Lake Materials Laboratory. All PiFM experiments were

excited by a pulsed quantum cascade laser (Block Engineering) with a gap-free narrow band tunable wave number of $760\text{--}1950\text{ cm}^{-1}$. The spectral linewidth is $\sim 2\text{ cm}^{-1}$ with a wave number resolution of 0.5 cm^{-1} . The PiFM experiment here was operated at the sideband excitation with the laser-frequency modulated at $f_m = f_1 - f_0$, where f_0 is the first mechanical eigen mode resonances of the cantilever that is used for PiF signal detection, while f_1 denotes the second ones recorded for the AFM topography of the sample. The probe is a Pt-coated tip with a resonant frequency of $\sim 350\text{ kHz}$ (PPP-NCHPt-MB, Nanosensors). The atomic force microscopy, Kelvin probe force microscopy (KPFM) and conductive atomic force microscopy (c-AFM) images were obtained by Bruker ICON2-SYS.

TOF-SIMS analysis was performed on a TOF-SIMS-M6 spectrometer (ION-TOF GmbH, Münster, Germany) equipped with a 30 keV Bi_3^+ primary ion gun pulsed at 10 kHz (mass range: $0 - 563\text{ Da}$). An argon gas cluster ion source (GCIB, 10 kV , 5 nA) was employed as sputter gun. Negative ion spectra were calibrated by O^- , OH^- , C_2^- , C_2H^- , and Cl^- , etc. An electron flood gun for charge neutralization was applied throughout the experiments. The scan sputter area was $400 \times 400\text{ }\mu\text{m}^2$ and the analysis area was $200 \times 200\text{ }\mu\text{m}^2$. Data were processed by ION-TOF SurfaceLab software (Version 7.4, ION-TOF GmbH) by signal of corresponding ions or fragment ions. To better resolve the SAM signal in TOF-SIMS, perovskite films with reduced thickness were prepared by diluting the perovskite precursor solution. To visualize the SAM layer more clearly, the perovskite precursor solution was diluted to form a thinner perovskite film.

Steady-state photoluminescence (PL) spectra were carried out with Horiba Jobin Yvon system. The excitation wavelength was set to 490 nm , and the final spectra were obtained by averaging three scans. The films tested in time-resolved photoluminescence (TRPL) were excited by a 485 nm pulse laser with a repetition frequency of 500 kHz provided by a picosecond pulsed diode laser (FLS980, Edinburgh Instruments Ltd). PL mapping experiments were undertaken by using a confocal laser scanning microscopy (CLSM, Leica STELLARIS 8, Germany) with a $40\times$ object lens. Perovskite films were excited with a Diode laser (488 nm), and the photoluminescence were collected from $600\text{--}700\text{ nm}$.

Nanosecond transient absorption spectrometer was composed of a regenerative-amplified Ti: sapphire laser system (Coherent) and EOS pump-probe system (Ultrafast Systems). The regenerative-amplified Ti: sapphire laser system (Legend Elite-1K-HE, center wavelength of 800 nm , pulse duration of 25 fs , pulse energy of 4 mJ , repetition rate of 1 kHz) was seeded with a mode-locked Ti: sapphire laser system (Vitara) and pumped with a Nd: YLF laser (Evolution 30). The output 800 nm fundamental of the amplifier was split into two beam pulses. The main part of the fundamental beam went through the optical parametric amplifiers (TOPAS-C), whose output light was set as the pump light with wavelength of 488 nm and chopped by a mechanical chopper operating at frequency of 500 Hz . Probe light was generated from an EOS (Ultrafast Systems) apparatus, produced in a diode-laser-pumped photonic crystal fiber, and electronically delayed relative to the pump pulse with a digital delay generator. Data acquisition was performed using the EOS software package from Ultrafast Systems. The pump was spatially and temporally overlapped with the probe beam on the sample.

Surface and cross-sectional morphology of the films and devices were examined by scanning electron microscopy (SEM, Hitachi S-4800). For the cross-sectional image, the sample was coated with ca. 1 nm -thick gold using sputter to enhance the conductivity.

Characterization of devices

The light intensity was calibrated to be $100\text{ mW}\cdot\text{cm}^{-2}$ by an SRC-2020 reference cell (traceable to NREL). The current density-voltage (J - V) curves of the perovskite solar cells were measured using a Keysight

B2901A Source-Meter, with the scanning voltage from 1.22 V to -0.2 V in 20 mV step and delay time of 1 ms . The device area is confined to 0.09 cm^2 by a mask. The measurements were performed in a glove box filled with nitrogen (oxygen and water contents are smaller than 10 ppm). Enli-tech class AAA Solar Simulator (model, SS-X180R-3A) with a 450 W xenon lamp was used as the light source. The EQE responses were measured by Solar Cell Spectral Response Measurement System QE-R3-011 (Enli Technology Co., Ltd., Taiwan). The light intensity at each wavelength was calibrated with a standard single-crystal Si photovoltaic cell. For the stability tests, all the devices were encapsulated, and measurement was performed under a LED that was adjusted to $AM\ 1.5\text{ G}$ ($100\text{ mW}\cdot\text{cm}^{-2}$) in ambient atmosphere.

Molecular simulations

Density functional theory (DFT) calculations were performed using the Vienna Ab initio Simulation Package (VASP). The projector augmented-wave (PAW) method was employed, and the Perdew–Burke–Ernzerhof (PBE) functional within the generalized gradient approximation (GGA) was used to describe the exchange–correlation interactions. A Vacuum layer of 30 \AA was used in the Z-direction to separate the slabs. The plane-wave cutoff energy was set to 600 eV . Structural relaxation was carried out using the conjugate gradient algorithm with an energy convergence criterion of $1 \times 10^{-4}\text{ eV}$ and a force convergence threshold of $0.05\text{ eV}/\text{\AA}$. The Brillouin zone was sampled using a Γ -centered $1 \times 1 \times 1$ k-point mesh due to the large size of the supercell. Subsequently, total energies were calculated on the optimized geometries using a denser Γ -centered $3 \times 3 \times 1$ mesh. VESTA was used for visualization.

The Molecular Dynamics simulation was performed using the Materials Studio (MS) 2020 software package (BIOVIA, USA). A model containing NiO, molecule MeOF-4PACz and molecule MeOF-4SHCz were built through Amorphous Cell (AC) modules with Condensed-phase Optimized Molecular Potentials for Atomistic Simulation Studies II (COMPASSII) the force field. The Forcite module was used to optimize the molecular structure, during the geometric optimization process, the convergence threshold for maximum energy change, maximum force convergence threshold, and maximum displacement convergence threshold are 0.001 kcal/mol , $0.5\text{ kcal/mol}/\text{\AA}$, and 0.015 \AA , respectively. To obtain a more optimized structure, a 100 ps dynamic simulation was conducted under the NVT ensemble with a step size of 1 fs . In the progress of MD, Electrostatic is calculated using Ewald, while van der Waals is calculated using atom based. The precise Nose-Hoover temperature control mode and Berendsen pressure control mode are used in the dynamic process.

Reporting summary

Further information on research design is available in the Nature Portfolio Reporting Summary linked to this article.

Data availability

Data supporting this study are available within the Article and Supplementary Information. Source Data Files are provided with this paper. Additional data are available from the corresponding author on request. Source data are provided with this paper.

References

- Zhang, G. et al. Suppressing interfacial nucleation competition through supersaturation regulation for enhanced perovskite film quality and scalability. *Sci. Adv.* **10**, ead16398 (2024).
- Liu, M. et al. Localized Oxidation Embellishing Strategy Enables High-Performance Perovskite Solar Cells. *Angew. Chem. Int. Ed.* **63**, e202318621 (2024).
- Qu, Z. et al. Enhanced charge carrier transport and defects mitigation of passivation layer for efficient perovskite solar cells. *Nat. Commun.* **15**, 8620 (2024).

- Jiang, X. et al. Isomeric diammonium passivation for perovskite–organic tandem solar cells. *Nature* **635**, 860–866 (2024).
- Zhang, Z. et al. Rationally designed universal passivator for high-performance single-junction and tandem perovskite solar cells. *Nat. Commun.* **16**, 753 (2025).
- Zhang, S. et al. Minimizing buried interfacial defects for efficient inverted perovskite solar cells. *Science* **380**, 404–409 (2023).
- Zhao, K. et al. peri-Fused polyaromatic molecular contacts for perovskite solar cells. *Nature* **632**, 301–306 (2024).
- Liu, S. et al. Buried interface molecular hybrid for inverted perovskite solar cells. *Nature* **632**, 536–542 (2024).
- Zhu, J. et al. Self-assembled hole-selective contact for efficient Sn–Pb perovskite solar cells and all-perovskite tandems. *Nat. Commun.* **16**, 240 (2025).
- Paniagua, S. A. et al. Phosphonic Acids for Interfacial Engineering of Transparent Conductive Oxides. *Chem. Rev.* **116**, 7117–7158 (2016).
- Suo, J. et al. The Dual Use of SAM Molecules for Efficient and Stable Perovskite Solar Cells. *Adv. Energy Mater.* **15**, 2400205 (2025).
- Koh, S. E. et al. Phenylphosphonic acid functionalization of indium tin oxide: Surface chemistry and work functions. *Langmuir* **22**, 6249–6255 (2006).
- Bermudez, V. M. et al. Functionalization of indium tin oxide. *Langmuir* **22**, 11113–11125 (2006).
- Pawsey, S. et al. Self-Assembly of Carboxyalkylphosphonic Acids on Metal Oxide Powders. *Langmuir* **18**, 5205–5212 (2002).
- Chen, F. et al. Effect of Anchoring Groups on Single-Molecule Conductance: Comparative Study of Thiol-, Amine-, and Carboxylic-Acid-Terminated Molecules. *J. Am. Chem. Soc.* **128**, 15874–15881 (2006).
- Li, E. et al. Bonding Strength Regulates Anchoring-Based Self-Assembly Monolayers for Efficient and Stable Perovskite Solar Cells. *Adv. Funct. Mater.* **31**, 2103847 (2021).
- Zhang, S. et al. Conjugated Self-Assembled Monolayer as Stable Hole-Selective Contact for Inverted Perovskite Solar Cells. *ACS Mater. Lett.* **4**, 1976–1983 (2022).
- Tang, H. et al. Reinforcing self-assembly of hole transport molecules for stable inverted perovskite solar cells. *Science* **383**, 1236–1240 (2024).
- Guo, H. et al. Neglected acidity pitfall: boric acid-anchoring hole-selective contact for perovskite solar cells. *Natl Sci. Rev.* **10**, nwad057 (2023).
- You, J. et al. Improved air stability of perovskite solar cells via solution-processed metal oxide transport layers. *Nat. Nanotechnol.* **11**, 75–81 (2016).
- Lv, Z. et al. Surface Property Regulation of a Magnetron-Sputtered NiO_x Hole Transport Layer for High-Performance Inverted Perovskite Solar Cells. *ACS Appl. Mater. Interfaces* **16**, 54272–54281 (2024).
- Yu, S. et al. Homogenized NiO_x nanoparticles for improved hole transport in inverted perovskite solar cells. *Science* **382**, 1399–1404 (2023).
- Li, Z. et al. Stabilized hole-selective layer for high-performance inverted p-i-n perovskite solar cells. *Science* **382**, 284–289 (2023).
- Chen, H. et al. Regulating surface potential maximizes voltage in all-perovskite tandems. *Nature* **613**, 676–681 (2023).
- Boyd, C. C. et al. Overcoming Redox Reactions at Perovskite-Nickel Oxide Interfaces to Boost Voltages in Perovskite Solar Cells. *Joule* **4**, 1759–1775 (2020).
- Yang, Y. et al. Inverted perovskite solar cells with over 2,000 h operational stability at 85 °C using fixed charge passivation. *Nat. Energy* **9**, 37–46 (2024).
- Li, J. et al. Enhancing the efficiency and longevity of inverted perovskite solar cells with antimony-doped tin oxides. *Nat. Energy* **9**, 308–315 (2024).
- Chen, Z. et al. Asymmetric Self-Assembled Monolayer as Hole Transport Layer Enables Binary Organic Solar Cells Based on PM6:Y6 with Over 19% Efficiency. *CCS Chem.* <https://doi.org/10.31635/ccschem.024.202404707> (2024).
- Tai, G. et al. Fast and large-area growth of uniform MoS₂ monolayers on molybdenum foils. *Nanoscale* **8**, 2234–2241 (2016).
- Mekhalif, Z., Riga, J., Pireaux, J.-J. & Delhalle, J. Self-Assembled Monolayers of n-Dodecanethiol on Electrochemically Modified Polycrystalline Nickel Surfaces. *Langmuir* **13**, 2285–2290 (1997).
- Kresse, G. & Furthmüller, J. Efficient iterative schemes for ab initio total-energy calculations using a plane-wave basis set. *Phys. Rev. B* **54**, 11169 (1996).
- Blöchl, P. E. Projector augmented-wave method. *Phys. Rev. B* **50**, 17953 (1994).
- Perdew, J. P., Burke, K. & Ernzerhof, M. Generalized gradient approximation made simple. *Phys. Rev. Lett.* **77**, 3865 (1996).
- Momma, K. & Izumi, F. VESTA: a three-dimensional visualization system for electronic and structural analysis. *J. Appl. Cryst.* **41**, 653–658 (2008).
- Grosvenor, A. P., Biesinger, M. C., Smart, R. S.t.C. & McIntyre, N. S. New interpretations of XPS spectra of nickel metal and oxides. *Surf. Sci.* **600**, 1771–1779 (2006).
- Li, B. et al. Suppressing Oxidation at Perovskite–NiO Interface for Efficient and Stable Tin Perovskite Solar Cells. *Adv. Mater.* **36**, 2309768 (2024).
- Li, D. et al. Co-adsorbed self-assembled monolayer enables high-performance perovskite and organic solar cells. *Nat. Commun.* **15**, 7605 (2024).
- Park, S. M. et al. Low-loss contacts on textured substrates for inverted perovskite solar cells. *Nature* **624**, 289–294 (2023).
- Kirchartz, T., Márquez, J. A., Stolterfoht, M. & Unold, T. Photoluminescence-Based Characterization of Halide Perovskites for Photovoltaics. *Adv. Energy Mater.* **10**, 1904134 (2020).
- Al-Ashouri, A. et al. Monolithic perovskite/silicon tandem solar cell with >29% efficiency by enhanced hole extraction. *Science* **370**, 1300–1309 (2020).
- Wetzelaer, G.-J. A. H. et al. Trap-assisted non-radiative recombination in organic–inorganic perovskite solar cells. *Adv. Mater.* **27**, 1837–1841 (2015).
- Wang, X. et al. Hot Carrier Dynamics and Charge Trapping in Surface Passivated β -CsPbI₃ Inorganic Perovskite. *J. Phys. Chem. Lett.* **12**, 6907–6913 (2021).
- Sheng, C. et al. Exciton versus Free Carrier Photogeneration in Organometal Trihalide Perovskites Probed by Broadband Ultrafast Polarization Memory Dynamics. *Phys. Rev. Lett.* **114**, 116601 (2015).
- Krückemeier, L. et al. Understanding Transient Photoluminescence in Halide Perovskite Layer Stacks and Solar Cells. *Adv. Energy Mater.* **11**, 2003489 (2021).

Acknowledgements

This work was supported by the National Key Research and Development Program of China (No. 2024YFB4205200) (L.M.), the Strategic Priority Research Program of the Chinese Academy of Sciences, Grant No. XDB 0520102 (L.M.), and the National Natural Science Foundation of China (Nos. 52173188) (L.M.).

Author contributions

L.M. conceived the idea, designed the experiments and cowrote the manuscript. M.Y. assisted in the conception of the idea, synthesized the materials, performed fabrication and characterization, analyzed characterization and wrote the manuscript. Y.W., M.L. and Z.L. participated in the solar cell fabrication and analysis of characterization. Z.C. and X.Li. participated in the synthesis of materials and analysis of the NMR and mass spectrometry. S.Q. help calculate the reaction energy. J.Z. performed PL mapping and TA measurements. Y.Z. performed TOF-SIMS

and analyzed data. J.L. helped with the measurements of TA. L.M. and Y.L. supervised the project. L.M., M.Y. and Y.L. wrote the manuscript. All authors contributed to the work.

Competing interests

The authors declare no competing interests.

Additional information

Supplementary information The online version contains supplementary material available at

<https://doi.org/10.1038/s41467-025-66421-4>.

Correspondence and requests for materials should be addressed to Lei Meng.

Peer review information *Nature Communications* thanks the anonymous, reviewer(s) for their contribution to the peer review of this work. A peer review file is available.

Reprints and permissions information is available at <http://www.nature.com/reprints>

Publisher's note Springer Nature remains neutral with regard to jurisdictional claims in published maps and institutional affiliations.

Open Access This article is licensed under a Creative Commons Attribution-NonCommercial-NoDerivatives 4.0 International License, which permits any non-commercial use, sharing, distribution and reproduction in any medium or format, as long as you give appropriate credit to the original author(s) and the source, provide a link to the Creative Commons licence, and indicate if you modified the licensed material. You do not have permission under this licence to share adapted material derived from this article or parts of it. The images or other third party material in this article are included in the article's Creative Commons licence, unless indicated otherwise in a credit line to the material. If material is not included in the article's Creative Commons licence and your intended use is not permitted by statutory regulation or exceeds the permitted use, you will need to obtain permission directly from the copyright holder. To view a copy of this licence, visit <http://creativecommons.org/licenses/by-nc-nd/4.0/>.

© The Author(s) 2025